# A Multiscale Numerical Study of Hurricane Andrew (1992). Part IV: Unbalanced Flows

DA-LIN ZHANG

*Department of Meteorology, University of Maryland, College Park, Maryland*

YUBAO LIU AND M. K. YAU

*Department of Atmospheric and Oceanic Sciences, McGill University, Montreal, Quebec, Canada*

(Manuscript received 6 August 1999, in final form 23 May 2000)

ABSTRACT

Despite considerable progress in understanding the hurricane vortex using balanced models, the validity of gradient wind balance in the eyewall remains controversial in observational studies. In this paper, the structure and development of unbalanced forces and flows in hurricanes are examined, through the analyses of the radial momentum and absolute angular momentum (AAM) budgets, using a high-resolution (i.e., $\Delta x = 6$ km), fully explicit simulation of Hurricane Andrew (1992).

It is found from the radial momentum budgets that supergradient flows and accelerations, even after temporal and azimuthal averaging, are well organized from the bottom of the eye center to the upper outflow layer in the eyewall. The agradient accelerations are on average twice greater than the local Coriolis force, and caused mainly by the excess of the centrifugal force over the pressure gradient force. It is shown by the AAM budgets that supergradient flows could occur not only in the inflow region as a result of the inward AAM transport, but also in the outflow region through the upward transport of AAM. The eyewall is dominated by radial outflow in which the upward transport of AAM overcompensates the spindown effect of the outflow during the deepening stage. The intense upper outflow layer is generated as a consequence of the continuous outward acceleration of airflows in the eyewall updrafts. In spite of the pronounced agradient tendencies, results presented here suggest that the azimuthally averaged tangential winds above the boundary layer satisfy the gradient wind balance within an error of 10%.

The analyses of instantaneous fields show pronounced asymmetries and well-organized wavenumber-2 structures of the agradient flows and forces in the form of azimuthally propagating vortex–Rossby waves in the eyewall. These waves propagate cyclonically downstream with a speed half the tangential winds near the top of the boundary layer and vertically upward. Agradient flows/forces and AAM transport in the eye are also discussed.

## 1. Introduction

Gradient-wind balance (GWB) models have been widely used in theoretical studies of tropical cyclones, and they have provided many fundamental insights into the dynamics of the hurricane vortex (e.g., Eliassen 1951; Schubert and Hack 1982; Shapiro and Willoughby 1982; Emanuel 1986, 1997; Shapiro and Montgomery 1993). However, the validity of GWB in hurricanes remains controversial in observational studies. For example, Gray and Shea (1973) documented systematic gradient unbalanced flows in the eyewall, especially near the radius of maximum wind (RMW), with some observed winds exceeding the gradient winds by 40%–50%! Such large supergradient winds were found at the lowest flight level near the top of the maritime boundary layer (MBL, i.e., 900 hPa) where the inflow air decelerates rapidly on approaching the RMW. Gray and Shea attributed this low-level supergradient flow to the ''overshoot'' of the inflow air in the MBL and the midlevel supergradient flows to the upward convective transport of horizontal momentum in the eyewall. In addition, they noted pronounced thermal wind imbalance in the eyewall; the observed radial thermal gradient was 2–5 times greater than what vertical shear would imply.

On the contrary, Willoughby (1990, 1991) found from numerous aircraft measurements that the GWB model is a good approximation to the *azimuthally averaged* tangential winds in the inner-core region, with a root-mean-square error of less than 1.5 m $s^{-1}$ above the MBL and below the upper outflow layer. Similar conclusions were also obtained by LaSeur and Hawkins (1963) and

*Corresponding author address:* Dr. Da-Lin Zhang, Department of Meteorology, University of Maryland, College Park, MD 20742-2425.
E-mail: dalin@atmos.umd.edu

Hawkins and Rubsam (1968). According to Willoughby (1990, 1991), agradient flows could only occur locally in response to intense convective bursts or radial acceleration in the MBL, but they should nearly vanish after the azimuthal average. Moreover, supergradient flows act to spin down the primary circulation, which would in turn diminish the unbalanced component (Willoughby 1991). In their comment and reply exchanges, these different conclusions have been attributed by their opponents to possible measurement errors leading to the calculated large unbalanced flows (Willoughby 1991) and the use of different averaging techniques in computing gradient winds (Gray 1991).

The GWB issue has some practical interest to the understanding of secondary circulations in tropical cyclones. Strictly speaking, there should be little systematic radial flow and vertical motion in the eyewall if the tangential flow is in GWB. Thus, the gradient wind imbalance is required to determine the intensity and structure of secondary circulations, which would in turn cause the intensity change of the primary circulation in hurricanes. For instance, radial outflows (inflows) tend to decrease (increase) the magnitude of tangential winds in the eyewall under the constraint of angular momentum conservation. On the other hand, the radial outflow in the eye could play an important role in transporting the air mass from the inner-core region outward to reduce the central pressure of the storm (Liu et al. 1999). Furthermore, earlier theoretical studies have hypothesized that weak subsidence in the eye is caused by advection of the eye air radially outward into the eyewall as a result of supergradient flows inside the RMW (Malkus 1958; Kuo 1959; Smith 1980). Nevertheless, recent theoretical studies of balanced dynamics suggest that much of the hurricane vortex evolution could be viewed as proceeding through a series of quasi-equilibrium (gradient) balanced stages (e.g., Smith 1980; Raymond 1992; Shapiro and Montgomery 1993). While the hurricane vortex has been extensively studied in the context of balanced dynamics, it is still uncertain to what extent GWB is a good approximation to a developing hurricane vortex, and how some unbalanced flows are generated and distributed in the inner-core regions of hurricanes.

The purpose of the present study is to address the above controversy through the analyses of radial momentum and absolute angular momentum (AAM) budgets, using a high-resolution (i.e., $\Delta x = 6$ km), fully explicit simulation of Hurricane Andrew (1992). This simulation was performed using a cloud-resolving version of the Pennsylvania State University–National Center for Atmospheric Research (PSU–NCAR) nonhydrostatic model [i.e., the fifth-generation Mesoscale Model (MM5)]. Liu et al. (1997, 1999, hereafter referred to as Part I and II), have shown that the MM5 reproduces reasonably well the track and intensity, as well as the structures of the eye, the eyewall, spiral rainbands, RMW, and other inner-core features as compared to available observations and the results of previous hurricane studies. Thus, the four-dimensional, dynamically consistent simulation results could be used here to reveal the inner-core unbalanced dynamics of the hurricane vortex. Because the storm was observed to intensify until landfall, the budget analyses so performed will reflect the dynamic characteristics of an intensifying hurricane. In this study, we attempt to address the following questions: To what extent is the GWB model a good approximation to the local and azimuthally averaged tangential winds in an intensifying hurricane? What causes the gradient wind imbalance locally and in an azimuthally averaged state? What is the intensifying mechanism of tangential winds in the eyewall?

The next section presents the budget equations for radial momentum and AAM in cylindrical coordinates and the axisymmetric structures of the simulated storm. Section 3 shows the processes leading to the intensification of tangential flows in the eyewall through the AAM budgets. Section 4 presents the radial force imbalance and evidence of local and azimuthally averaged unbalanced flows in the hurricane vortex. Because Andrew is a very compact storm with a small eye, more attention will be given to the budget analyses in the eyewall. A summary and concluding remarks are given in the final section.

## 2. Budget equations and inner-core structures

All budget calculations are based on the governing equations used in the MM5 (see Dudhia 1993; Grell et al. 1995). In the model, all prognostic variables are written in the mass-weighted (i.e., $p^* = p_s - p_t$) flux form with a vertical $\sigma$ coordinate on Mercator map projection, where $p_s$ and $p_t$ are the pressure at the bottom and the top of the model, respectively. Because of the dominant axisymmetric nature of hurricanes, it is convenient to discuss the inner-core dynamics in cylindrical $(r, \lambda, z)$ coordinates, where $r$ is the radius from the vortex's surface minimum pressure pointing outward, $\lambda$ is the azimuthal angle, and $z$ is the vertical height axis. See Part II for a detailed description of the transformation between the MM5 $(x, y, \sigma)$ and cylindrical coordinates.

The governing equation in cylindrical coordinates for radial momentum can be written as

$$\frac{dU}{dt} = -\frac{1}{\rho}\frac{\partial p}{\partial r} + \frac{V^2}{r} + fV + 2\Omega \cos\phi W \cos\lambda + U_D, \tag{1}$$

where

$$\frac{d}{dt} = \frac{\delta}{\delta t} + U'\frac{\partial}{\partial r} + \frac{V'}{r}\frac{\partial}{\partial \lambda} + W\frac{\partial}{\partial z}; \tag{2}$$

$W$, $U$, and $V$ are, respectively, the vertical, radial, and azimuthal winds relative to the earth in cylindrical coordinates; $\Omega$ is the angular velocity of the earth; and $\phi$ is the latitude. To separate the advective effects asso-

ciated with the storm movement from the dynamical processes that influence the storm development, we define $\partial/\partial t = \partial/\partial t + \mathbf{C} \cdot \nabla$ as the local tendency, where $\mathbf{C}$ is the velocity of the storm's movement, and $U'$ and $V'$ are the horizontal wind components relative to the storm. Equation (1) states that the radial acceleration is determined by the radial pressure gradient force ($PGF_R$; $U_p$), the centrifugal force ($U_E$), the Coriolis force ($U_C$) including the effects of vertical motion, and the effect of the MBL plus numerical diffusion ($U_D$). As will be seen in section 4, $U_E$ and $U_C$ play an important role, but to different degrees, in coupling the tangential and radial components of motion through $PGF_R$ in hurricanes.

Similarly, the governing equation for azimuthal momentum in cylindrical coordinates can be written as

$$\frac{dV}{dt} = -\frac{1}{\rho}\frac{\partial p}{r\partial\lambda} - \frac{UV}{r} - fU + 2\Omega \cos\phi W \sin\lambda + V_D. \quad (3)$$

It is more convenient to rewrite Eq. (3) in terms of a prognostic equation in AAM defined by

$$M = r(V + fr/2), \quad (4)$$

with the form

$$\frac{dM}{dt} = -\frac{1}{\rho}\frac{\partial p}{\partial\lambda} + 2r\Omega \cos\phi W \sin\lambda + \frac{r^2}{2}v_m\beta + rV_D, \quad (5)$$

where $\beta$ is the variation of the Coriolis parameter with latitude and $v_m$ denotes the projections of $U$ and $V$ onto the longitudinal axes, and it is actually the $y$ component of the MM5's horizontal flow in the Mercator projection. We can see that the Lagrangian rate of changes in AAM arises from a pressure torque ($M_p$), a longitudinally oriented Coriolis torque due to vertical motion, a beta torque, and a torque due to numerical diffusion and the MBL effects. Our calculation indicates that the last three terms on the right-hand side of Eq. (5) are one to two orders of magnitude smaller than the pressure torque in the eyewall except for the frictional effects in the MBL (see Fig. 2a for their azimuthally averaged structures). Thus, AAM is near-conserved above the MBL if the hurricane is axisymmetric.

In the present case, the above budget terms are obtained directly from the MM5 outputs over the fine-mesh domain at 5-min intervals from the 56–57-h integration, valid at 2000–2100 UTC 23 August 1992. During this period, the storm reaches a maximum surface wind of 68 m s$^{-1}$ and a minimum surface central pressure of 935 hPa (see Fig. 2 in Part I). Each budget term, rather than each variable, is then transformed from the model ($x$, $y$, $\sigma$) to cylindrical coordinates with the surface minimum pressure of the storm at the origin. For most of the results presented herein, each budget term is averaged azimuthally (for each 5-min dataset) and temporally over the 1-h period (see Part II for how to perform the azimuthal average). With the azimuthal averaging the pressure torque and the azimuthal advection terms vanish. The horizontal winds relative to the storm required in the advection terms are obtained by subtracting out the storm's movement at an easterly speed of 7.5 m s$^{-1}$.

For the convenience of subsequent discussions, Fig. 1 shows radius–height cross sections of the temporally and azimuthally averaged vertical motion ($W$), radial ($U$), and tangential ($V$) flows; AAM; and equivalent potential temperature $\theta_e$. In general, the flow structures are very similar, albeit slightly stronger in intensity due to the use of much shorter time averaging, to those given in Fig. 3 of Part II. The eyewall is characterized by an intense slantwise updraft (UP) and a pronounced divergent outflow layer in the upper troposphere. The low-level inflowing air, which is peaked at the surface near $R = 40$ km (>27 m s$^{-1}$), turns sharply out- and upward partly into the eyewall and partly into the outer region after passing the RMW (Figs. 1a,b). These two airstreams are induced by the eyewall convection and surface friction (Willoughby 1979), respectively, forming an ascending outflow jet (>10 m s$^{-1}$) across the eyewall in the lowest 3-km layer. Moreover, the ascending air in the eyewall experiences continued outward acceleration until the upper outflow layer. This radial acceleration accounts for *the outward cyclonic rotation* of streamlines in a deep layer in the inner-core region (see Fig. 16 in Part I). In the outer regions, there is a radial inflow at the melting level, with weak outflows occurring above and below. On average, the radial flow in the eye is inward above $z = 9$ km and outward below, with some mass subsiding in a narrow zone (DN) at the inner edge of the eyewall down to the MBL. The mean axisymmetric tangential flow exhibits a ring of intense flow that is maximized (i.e., $V_{max} = 75$ m s$^{-1}$) at a radius of 30 km and an altitude of 800 m (Fig. 1c); it also coincides with the ascending outflow jet. The axis of the RMW lies outside the intense slantwise updrafts (UP), and slopes outward up to 10 km. The surface friction causes extremely large vertical shears in the MBL, particularly in the eyewall.

The mean AAM about the central axis of the storm, following the secondary circulation, shows significant inward decreases in magnitude with a large vertical gradient in the MBL as a result of the surface friction, and outward increases in the upper outflow layer as a result of advection (Fig. 1d). The eyewall is marked by dense sloping AAM surfaces that flatten in the upper outflow layer. In the eyewall, the AAM surfaces and the equivalent potential temperature $\theta_e$ surfaces are nearly parallel, suggesting the presence of a state of conditional symmetric neutrality (Emanuel 1986), as discussed in Zhang et al. (2000). Note the inward ''buckling'' of AAM in the vicinity of $V_{max}$ that plays an important role in the spinup of the eyewall discussed below.

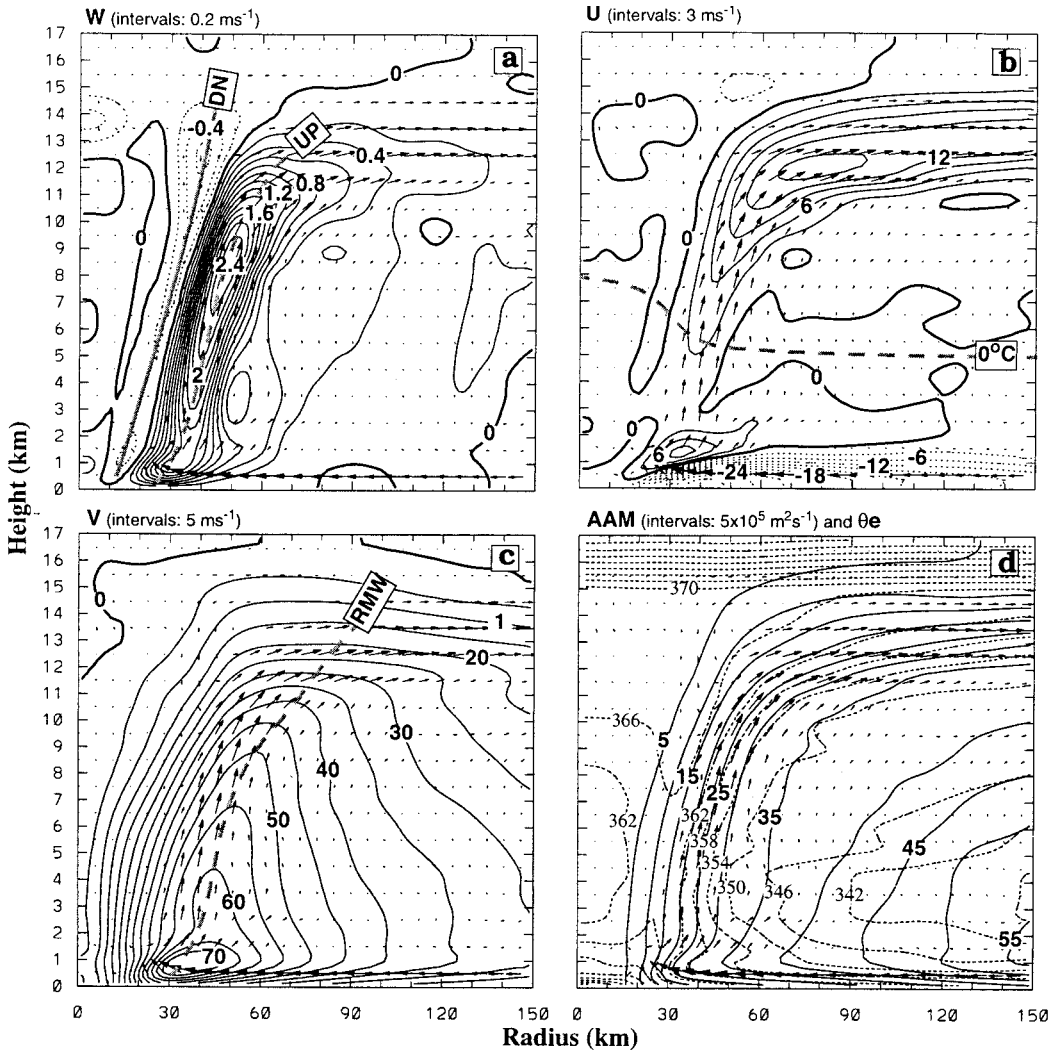


FIG. 1. Radius–height cross sections of the hourly and azimuthally averaged (a) vertical velocity ($W$) at intervals of 0.2 m s$^{-1}$, (b) radial winds ($U$) at intervals of 3 m s$^{-1}$, (c) tangential winds ($V$) at intervals of 5 m s$^{-1}$, and (d) absolute angular momentum (AAM, solid) at intervals of $5 \times 10^5$ m$^2$ s$^{-1}$ and equivalent potential temperature ($\theta_e$, dashed) at intervals of 4 K, superposed with the cross-sectional flow vectors, taken from the 56–57-h integration or the period 2000–2100 UTC 23 Aug 1992. The radius of maximum wind, and the axes of the eyewall updrafts and the inner-edge downdrafts are represented by RMW, UP, and DN, respectively.

## 3. Absolute angular momentum transport

To facilitate the understanding of radial momentum budgets given in the next section, we first examine the AAM budgets to gain insight into the mechanism for intensification of the tangential flows in the inner-core regions. The net Lagrangian tendency (Fig. 2a) is essentially the sources/sinks of AAM associated with numerical diffusion and boundary layer processes since the pressure torque nearly vanishes after the azimuthal average and the other two terms on the right-hand side of Eq. (5) are very small. Horizontal diffusion acts to smooth the large horizontal AAM gradients across the eyewall, decreasing the local AAM in the eyewall and increasing it inward (cf. Figs. 1d and 2a). However, the diffusive influence in the eye is at least one order of magnitude smaller than the advection terms. Vertical turbulence mixing is a small source above the buckled layer of AAM in the vicinity of $V_{max}$. In contrast, the surface layer is a distinct sink of AAM. The sink increases rapidly toward the RMW because the frictional dissipation is proportional to the square of the tangential winds. It is apparent that (a) the two-dimensional AAM is nearly conserved above the MBL, and (b) an excess of AAM has to be transported from the environment into the eyewall to overcompensate the dissipation by surface friction if the hurricane were to intensify.

Using the conservative property of AAM, we may study the intensification of the tangential flow in terms of the advection of AAM. Clearly, the distribution of AAM implies that horizontal advection by the major

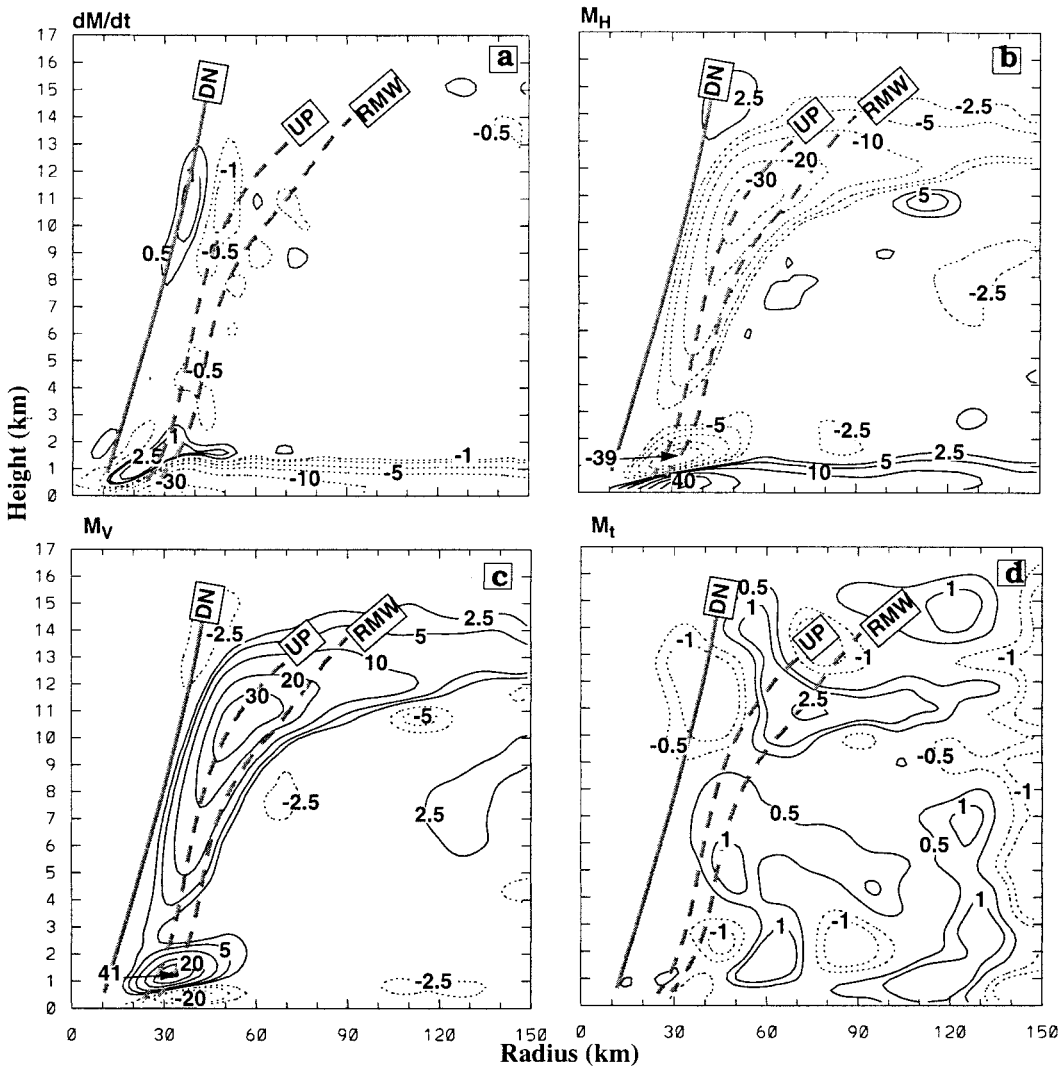


FIG. 2. As in Fig. 1 but for the AAM budget: (a) the net Lagrangian tendency due to all the sources/sinks ($dM/dt$), (b) the horizontal advection ($M_H$), (c) the vertical advection ($M_V$), and (d) the local tendency ($M_t$). Both (a) and (d) are contoured at $\pm 0.5$, $\pm 1$, $\pm 2.5$, $\pm 5$, $\pm 10$, $\pm 20$, and $\pm 30 \times 10^5$ m$^2$ s$^{-1}$ h$^{-1}$ while (b) and (c) are contoured at $\pm 2.5$, $\pm 5$, $\pm 10$, $\pm 20$, $\pm 30$, and $\pm 40 \times 10^5$ m$^2$ s$^{-1}$ h$^{-1}$.

inflow in the MBL would increase the AAM of the storm (cf. Figs. 1d and 2b). The increase is especially rapid toward the RMW as both the radial and tangential winds become large. This radial transport appears to exceed the frictional dissipation during this intensifying stage (cf. Figs. 2a,b), and it accounts for the rapid increase of the localized tangential flow (i.e., $V_{max}$) near the top of the MBL (Figs. 1c,d). As will be shown in the next section, the rapid spinup results from the overshoot of the inflow air, leading to the inward buckling of AAM near the top of the MBL (Fig. 1d). This buckled AAM becomes an important source through vertical transports for the spinup of tangential flows in the eyewall above the MBL. By comparison, the general radial outflow above, albeit a few meters per second, tends to reduce AAM everywhere in the eyewall, especially in the upper outflow layer. It can be estimated from Eq. (3) that the low-level 8–10 m s$^{-1}$ outflow jet in the vicinity of $V_{max}$ could spin down the peak wind of $\sim$75 m s$^{-1}$ to half of its value in roughly 35–45 min. However, the above figure becomes quite different when vertical advection of AAM is included. For example, Fig. 2c shows that vertical advection transports AAM upward in the eyewall and outward in the outflow layer. Of importance is that in the eyewall above $z = 3.5$ km the vertical advection term is slightly greater than but opposite in sign to the horizontal advection. Therefore, with a deep layer of outflow, the amplification of the tangential flows in the eyewall depends critically on the excess of upward transport of AAM over that of horizontal transport above the MBL.

The net result is that the local AAM tendency above

the MBL is a small residue between the radial and vertical advections (Fig. 2d). Notwithstanding small, there is clear evidence of the slow spinup of the eyewall below the upper outflow axis, with an average local tangential wind tendency of 1–2 m $s^{-1}$ $h^{-1}$ at the RMW. Above the upper outflow axis where the tangential flow is weak (Figs. 1b,c), local AAM tends to decrease (increase) in the outflow (inflow) region. Except near the top of the MBL and in the upper troposphere, the local AAM tendency in the eye is very small due partly to the weak tangential flow and partly to the small radius (as an ''amplification'' factor). The upper-level negative tendency is evidently caused by the downdrafts (DN) near the inner edge of the eyewall. They tend to spin down locally the rotation of the eye, as is evident from the more horizontally oriented isotachs (cf. Figs. 1c and 2d). The significant local tendencies near the radius of 125 km are related to a principal rainband. However, the corresponding changes in local tangential winds are much smaller than those in the inner-core region due to the large amplification factor by radius.

To see how representative the above axisymmetric transport of AAM is, Figs. 3–5 show the *slanting* azimuth–height cross sections of the AAM budgets and radial flows in the eyewall and eye. Note the increase in horizontal length scale with height that has the ratios of 7:3 for the eyewall and 4:1 for the eye between the top and bottom boundaries due to the rectangular mapping of a trapezoidal surface associated with the slanting cross sections. It is apparent that the AAM transport above the MBL is highly asymmetric, and strongly influenced by the downshear-tilted, ''wavenumber 1'' inflows/outflows in the inner-core region (cf. Figs. 3–5). Of importance is that *more air is outgoing than incoming in the eyewall,* consistent with the result obtained from the azimuthal average (cf. Figs. 3a and 1b). *The localized radial flows are relatively weak in the eye due to the presence of large inertial stability,* except above the upper-level outflow layer where the radial and tangential winds are comparable in magnitude. As indicated in Zhang et al. (2000, hereafter referred to as Part III), the eyewall updrafts tend to be relatively weak (strong) in the inflow (outflow) region due to the reduced (enhanced) buoyancy associated with the inward (outward) advected lower- (higher-) $\theta_e$ air. For the same reason, the inflow air appears to be favorable for the development of downdrafts in the eye, particularly above the upper outflow layer (see Part III for more details). All these features can also be inferred from the in-plane flow vectors and $\theta_e$ structures displayed in Figs. 3 and 1d.

Because of the large AAM gradient across the eyewall, its horizontal transport is dominated by the radial component, with the result that the local AAM increases (decreases) in the inflow (outflow) region (cf. Figs. 4a and 1d). While the inflows advect higher AAM inward, they do not transport significant AAM vertically in the eyewall due to their associated weak vertical motion (Fig. 4b). In contrast, intense updrafts in the *outflow* region tend to advect pronounced AAM upward. Like their azimuthal average, the local AAM sources/sinks are small compared to the advections (cf. Figs. 4a, 4b, and 4d), except in the MBL; so AAM is also near-conserved three-dimensionally in the eyewall. As a result, the local tendency shows an increase of AAM in both the inflow and outflow regions with the latter having intense updrafts (Fig. 4c). Wherever the updraft is weak, of course, the local tendency in the outflow region becomes negative due to its spindown effect. Nevertheless, the upward transport in the outflow region appears to more than offset the negative radial transport for the local increases in AAM over most of the eyewall.

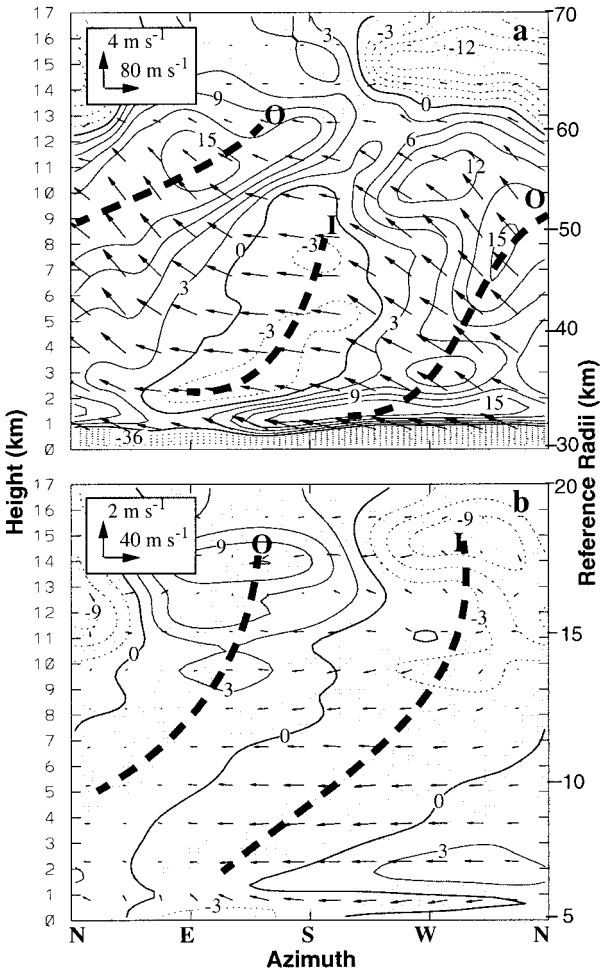


FIG. 3. The azimuth–height cross sections of the temporally averaged system-relative radial flow (every 3 m $s^{-1}$) with the downdrafts shaded that are taken along the *slanting surfaces* (a) in the eyewall (i.e., from $R$ = 30 km at the surface to $R$ = 70 km at the 17-km height), and (b) in the eye (i.e., from $R$ = 5 km at the surface to $R$ = 20 km at the 17-km height) from the 56–57-h integration. The right axes show the radius in km at a few selected heights. Thick dashed lines denote the axes of incoming (I) and outgoing (O) air. Solid (dashed) lines are for positive (negative) values. In-plane flow vectors are superposed.

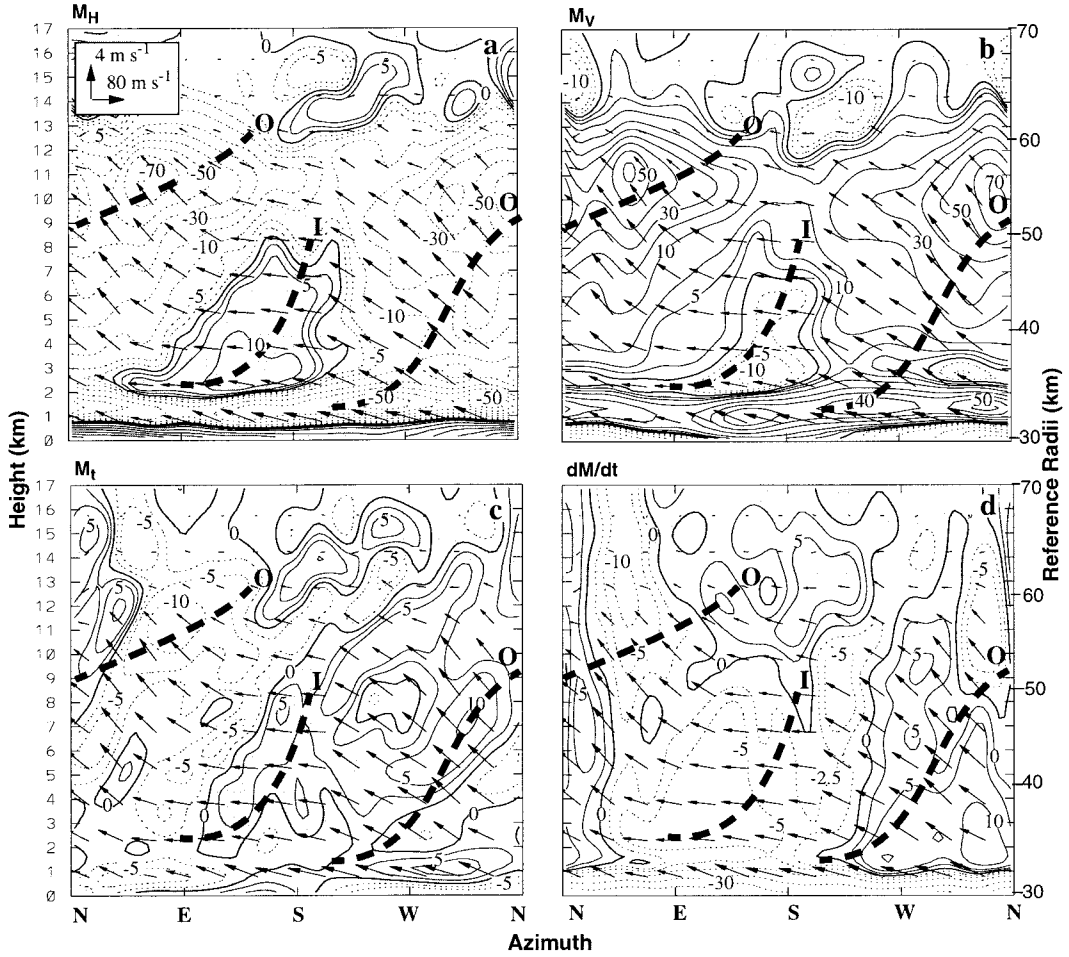


FIG. 4. As in Fig. 3a but for the AAM budget in the eyewall: (a) horizontal advection ($M_H$) with the inflow shaded, (b) vertical advection ($M_V$) with the downdraft shaded, (c) local tendency ($M_t$) with the inflow shaded, and (d) Lagrangian tendency ($dM/dt$), contoured at 0, ±2.5, ±5, ±10, ±20, ±30, ±40, and ±50 × $10^5$ m$^2$ s$^{-1}$ h$^{-1}$.

This result is consistent with the conclusion obtained from the azimuthal-averaged budget. In the lowest 2-km layer, the local rate of changes in AAM is determined by the sum of frictional dissipation, horizontal and vertical transports that are distributed relatively uniformly along the azimuthal direction. It follows that *the tangential flow in the eyewall could intensify not only in the inflow air as a result of the radial AAM transport, but also in the ascending outflow air through the upward AAM transport by intense updrafts.*

The AAM budgets in the eye are quite different from those in the eyewall (cf. Figs. 4 and 5), except for the horizontal transport by radial flows. For example, the vertical transport of AAM by general descent is so weak that it could be omitted in the budgets (Fig. 5b). However, the sources/sinks of AAM, dominated by the azimuthal pressure torque, are no longer negligible as compared to horizontal advection (cf. Figs. 5a and 5d). Of interest is that the AAM sources (sinks) occur in the west (east) semicircle below $z = 7$ km; they are shifted to the south (north) semicircle aloft (Fig. 5d). Similar patterns also occur in the eyewall (Fig. 4d). This distribution of sources and sinks coincides with that of the intensifying convection (see Figs. 5, 6, and 9 in Part I), suggesting that *the convectively generated asymmetry in the pressure torque in the eyewall has a significant impact on the AAM budget in the eye.* Thus, the local rates of AAM changes in the eye (or the rotation of the eye) appear to be more or less determined by the AAM sources/sinks (i.e., asymmetries in pressure torque plus diffusive processes) and modulated by the radial transport (Fig. 5c). This result appears to differ somewhat from the inward turbulence transport of AAM in the eye as hypothesized by Malkus (1958) and Kuo (1959).

It should be pointed out that the above-mentioned features associated with the radial inflows/outflows undergo rotation, roughly at the rate of one cycle in 1.5–2 h. This aspect will be discussed in the next section in association with the azimuthal propagation of vortex–Rossby waves in the eyewall.

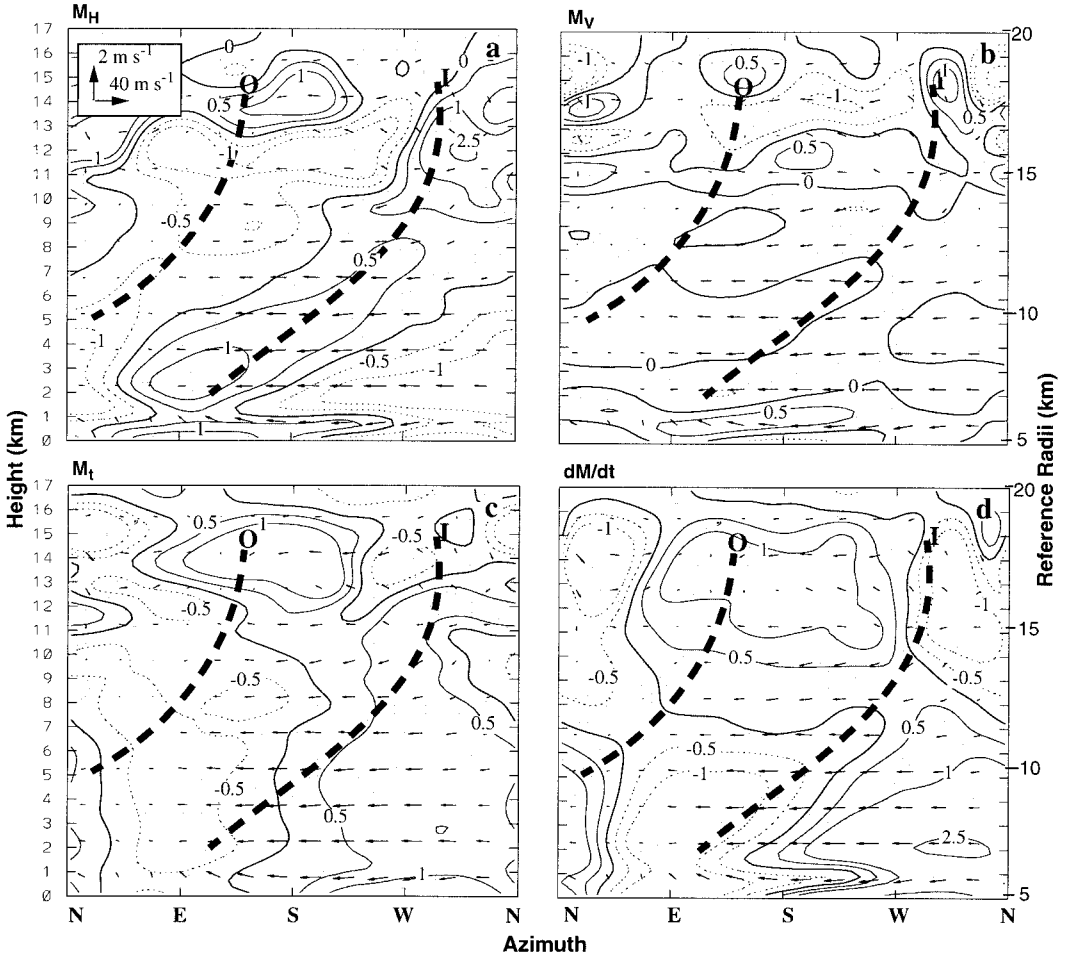


FIG. 5. As in Fig. 3b but for the AAM budget in the eye: (a) horizontal advection ($M_H$), (b) vertical advection ($M_V$), (c) local tendency ($M_t$), and (d) Lagrangian tendency ($dM/dt$), contoured at 0, ±1, ±2.5, ±5, and ±10 × $10^5$ m$^2$ s$^{-1}$ h$^{-1}$. Radial inflows are shaded in (a) and (c), and downdrafts are shaded in (b) and (d).

## 4. Unbalanced dynamics

With the AAM budgets presented above, we proceed to the analyses of unbalanced forces and flows in the simulated hurricane. Figure 6 shows all the radial budget terms in Eq. (1) and the extent of different approximations. Although the minimum pressure is located at the center of the storm, the most intense $PGF_R$ ($U_p$) occurs in the eyewall and its axis follows closely that of the RMW, except in the lowest 2 km (cf. Figs. 6a and 1c). Moreover, $PGF_R$ always points inward, and decreases rapidly with height. Clearly, this negative $PGF_R$ accounts for the generation of radial (frictional) inflow in the MBL that increases toward the RMW. However, $PGF_R$ could not explain the accelerating radial outflow aloft in the eyewall and in the upper troposphere (Fig. 1b). Thus, some other processes must play an important role in determining the vertical profiles of the radial outflow.

One of the major radial forces that counteracts $U_p$ is the centrifugal force $U_E$, which is similar in structure but opposite in sign to $U_p$, except in the lowest 2 km (cf. Figs. 6a,b). The sum of $U_p$ and $U_E$ shows the degree of cyclostrophic force imbalance ($U_{PE} = U_p + U_E$; see Fig. 6c). Apparently, $U_E$ overcompensates $U_p$ from the bottom of the eye center to the upper portion of the eyewall. This overcompensation gives rise to systematic supercyclostrophic acceleration[1] with its ridge axis coinciding with that of the sloping updrafts except for the layers below $z = 3$ km. The relative cyclostrophic force imbalance, defined as $I_c = U_{pE}/U_p = -r\,U_{pE}/V_c^2$, varies between ±6% from $z = 2$ km to 20% at $z = 10$ km in the updraft core regions (cf. Figs. 6a,c). However, the

[1] The supercyclostrophic (supergradient) acceleration or force is defined herein as the positive Lagrangian tendency of radial momentum (i.e., $dU/dt$), whereas the supercyclostrophic (supergradient) flow refers to an azimuthal wind that is greater than the cyclostrophic (gradient) wind and *tends to induce a radial outflow in the eyewall.* The opposite is implied for the subcyclostrophic (subgradient) acceleration and subcyclostrophic (subgradient) flow.

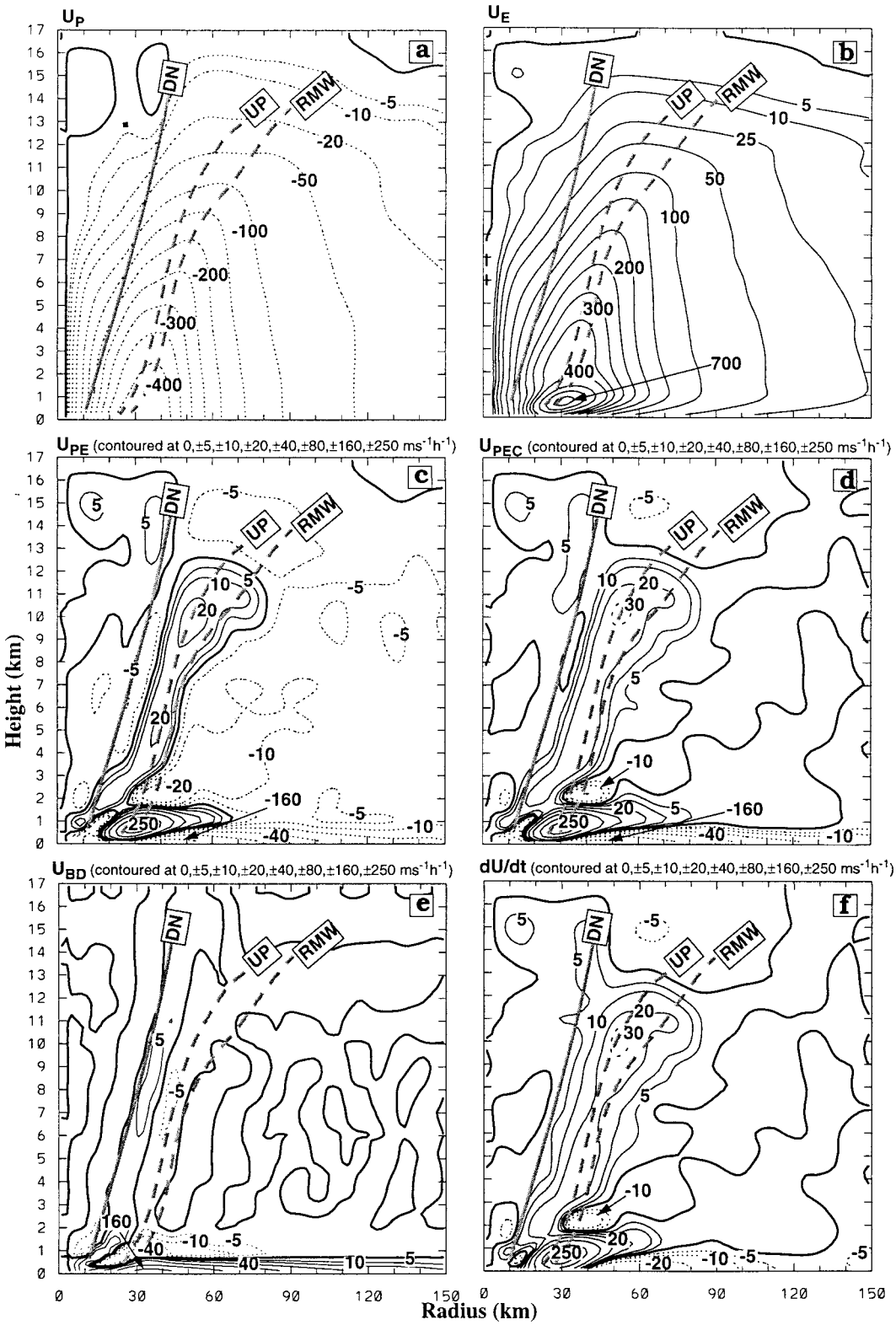


FIG. 6. As in Fig. 1 but for the radial momentum budget (unit: m $s^{-1}$ $h^{-1}$): (a) the radial pressure gradient force ($PGF_R$, $U_p$), (b) the centrifugal force ($U_E$), (c) the cyclostrophic force imbalance ($U_{PE} = U_p + U_E$), (d) the gradient force imbalance ($U_{PEC} = U_{PE} + U_C$), (e) the diffusion and boundary layer effects ($U_B$), and (f) the Lagrangian tendency ($dU/dt$).

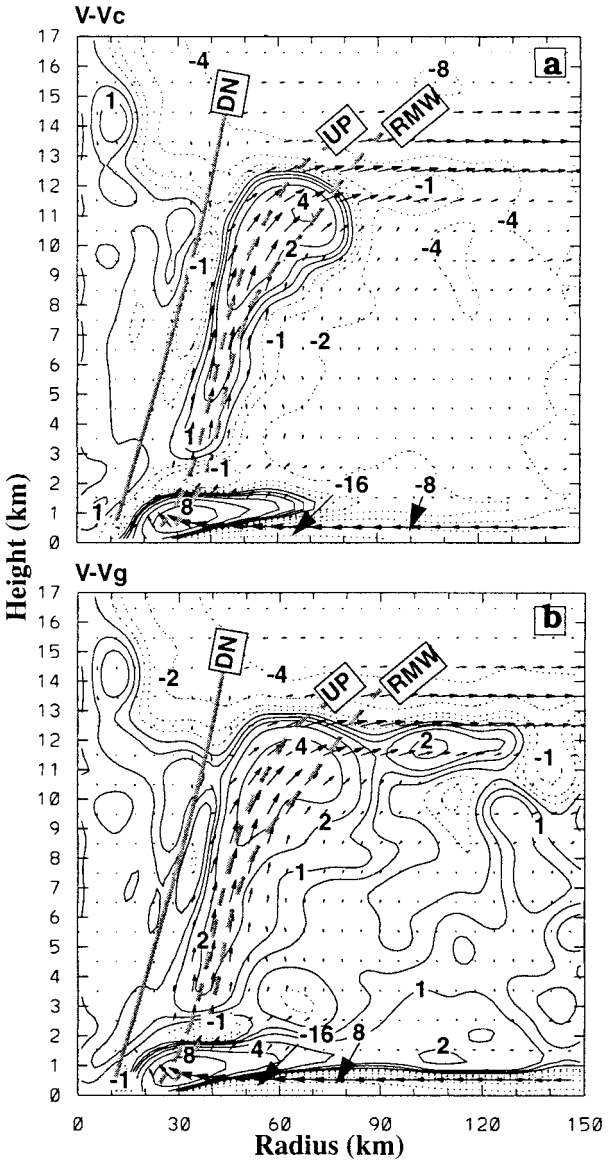


FIG. 7. As in Fig. 1 but for (a) acyclostrophic winds ($V - V_C$), and (b) agradient winds ($V - V_g$), contoured at 0, ±0.5, ±1, ±2, ±4, ±8, and ±16 m s$^{-1}$. In-plane full-flow vectors are superposed.

cyclostrophic winds ($V_c$) differ from the simulated winds ($V$) only by $-1$ to 3 m s$^{-1}$ in that layer (Fig. 7a) with the relative errors ranging from 3% to 9%. These two different measures of cyclostrophic imbalance could be seen from the following quadratic relationship between $V$ and $I_c$:

$$V = \sqrt{r(-U_p + U_{\mathrm{PE}})} = V_C\sqrt{1 - I_C}$$
$$\approx V_C(1 - I_C/2), \quad (6)$$

where $I_c \ll 1$ has been assumed. Equation (6) indicates that despite the pronounced acyclostrophic forces (e.g., $I_c = 20\%$), cyclostrophic winds could still be a good approximation, with an error of less than 10%, to the azimuthally averaged tangential winds above the MBL. These different results are obtained *because of the squared-difference relationship between the acyclostrophic acceleration and wind* [i.e., $U_{\mathrm{pE}} = (V^2 - V_c^2)/r$], which differs from the quasigeostrophic case where ageostrophic flow and acceleration are linearly related. Note that the cyclostrophic imbalance is substantially smaller and even close to null at the RMW. Of significance is the extremely large supercyclostrophic acceleration (i.e., >250 m s$^{-1}$ h$^{-1}$) in the vicinity of $V_{\max}$ that interrupts the large subcyclostrophic inflow in the MBL, and that appears to account for the development of the low-level radial outflow jet exceeding 9 m s$^{-1}$ near the RMW (cf. Figs. 6c and 1b). Clearly, *it is the centrifugal force (or inertial stability) that prevents the low-level radial inflow from reaching the eye, and vents the air from the bottom of the eye to maintain the mass balance.*

The degree of gradient force imbalance $U_{\mathrm{pEC}}$ ($=U_p + U_E + U_c$) can be evaluated by adding the Coriolis force ($U_c$) to $U_{\mathrm{pE}}$. Since $U_c$ is small but positive, it offers little offset to $U_p$ except in the far environment (not shown). In fact, the maximum value that $U_c$ could reach (i.e., $fV_{\max}$) is about 16.5 m s$^{-1}$ h$^{-1}$, which is less than 5% of the maximum value of $U_p$ or $U_E$. This result is consistent with the notion that the inner core is a region of high Rossby number flow in which $U_p$ is much greater than $U_c$. Therefore, the effect of adding $U_c$ on the distribution of the cyclostrophic imbalance is less significant in the inner-core region than that in the outer region (cf. Figs. 6c,d). Nevertheless, the cyclonic flows above the MBL in the eye, eyewall, and most outer regions all experience outward accelerations after including $U_c$.

A number of notable features are worth discussing. First, *even though the gradient force imbalance is a small difference between two large terms (i.e., $U_p$ and $U_E$), it is highly organized in the eyewall from the bottom of the eye center to the upper outflow layer.* Supergradient tendencies range from 20 to 30 m s$^{-1}$ h$^{-1}$ above $z = 3$ km, with the ridge axis *coinciding with that of the sloping updraft core rather than the RMW.* The supergradient tendencies are consistent with the increase in mean radial outflow with height in the sloping eyewall until the upper outflow layer where the supergradient acceleration decreases outward. Thus, air parcels accelerate outward as they ascend in the eyewall with their maximum acceleration in the core of the eyewall updrafts. In this sense, the intense radial outflow in the upper troposphere results from the continuous acceleration of the airflows as they rise in the eyewall, and a deep layer of supergradient acceleration is required for the development of the upper-level intense radial outflow. It is of importance that contrary to what was previously hypothesized (e.g., Willoughby 1979) GWB is a valid approximation in the upper outflow layer slightly beyond the RMW, where the radial and azimuthal flows are comparable in magnitude. Within the RMW, the upper-level outflows are not significantly dif-

ferent from the midlevel outflows in the context of supergradient acceleration (Fig. 6d).

Second, like the cyclostrophic force imbalance, an extremely intense supergradient acceleration occurs in the vicinity of $V_{max}$ in association with the outflow jet. The acceleration exceeds 250 m $s^{-1}$ $h^{-1}$—a value more than ⅓ of the centrifugal force (cf. Figs. 6b,d). The corresponding supergradient wind of greater than 12 m $s^{-1}$ suggests that more than ⅙ of the tangential wind in the vicinity of $V_{max}$ is unbalanced with the local Coriolis force and $PGF_R$ (Fig. 7b). This result confirms the significant supergradient flows observed at 900 hPa near the RMW (more likely in the outflow jets) by Gray and Shea (1973). Clearly, such intense supergradient acceleration would act as a brake on the friction-induced inflow in the MBL. Since this large imbalance is caused by the inward transport of AAM, based on the results shown in section 3, *this low-level supergradient outflow jet results from the overshoot or deceleration of the friction-induced inflowing air* (Gray and Shea 1973; Willoughby 1979). Note that the supergradient flow begins from the bottom of the eye center and then tilts into the eyewall (cf. Figs. 1b and 7b). As discussed in Part II, this branch of supergradient outflow plays an important role in (a) venting the air mass out of the eye to reduce the central pressure, and (b) transporting high-$\theta_e$ air from the bottom of the eye to support eyewall convection.

Third, the lowest 1-km airflows outside the RMW and over part of the bottom of the eye are highly subgradient as a result of the reduction of tangential flows by surface friction. Thus, $PGF_R$ is the driving force to accelerate the environmental high-$\theta_e$ air in the MBL into the eyewall.

Fourth, agradient tendencies are also present in the eye, although they are weak, due mainly to the local AAM sources and its inward transport (cf. Figs. 5 and 6d) and less to the effect of the flow asymmetry. They are generated in a weak return inflow above $z = 8$ km and a weak outflow below (cf. Figs. 5d and 1b). Note a layer of weak subgradient tendency above the axis of the upper outflow layer that results from the rapid decrease of tangential winds (or $U_E$) as the air rotates outward under the constraint of conservation of AAM. It is this subgradient tendency that drives the upper return inflow into the eye. Of interest is that the super- and subgradient tendencies are interfaced near the descending flow (DN) at the inner edge of the eyewall, indicating that this descending zone is fed by this return inflow.

It should be pointed out that while our low-level gradient imbalance results are in agreement with those found at 900 hPa by Gray and Shea (1973), the other results do not contradict those of Willoughby's (1990). Specifically, Willoughby's GWB conclusions were mostly drawn from the aircraft observations taken at 850 and 700 hPa where the agradient tendencies happen to be relatively weak, according to our model simulation (see Figs. 6d and 7b). However, his Fig. 1a does show some pronounced departures from GWB at 900 hPa, like those shown in Fig. 6d, even during the decaying stage of a tropical storm. Thus, the different results between Willoughby's work and Gray and Shea's work do not seem to be attributable to the different averaging techniques used or measurement errors, but to the levels of observations they analyzed. At this point, one should note the *two different ways to view gradient imbalance*: one is based on the magnitude of *unbalanced (agradient) forces* or tendencies as given in Eq. (1) and the other on the *departures from gradient winds* ($V_G$) or unbalanced (agradient) flows as used in almost all of the previous studies. Based on Eq. (6), we can see that the relative gradient unbalanced forces (i.e., $I_G = U_{PEC}/U_p$) would be about twice as large in magnitude than the relative gradient wind errors [i.e., $(V - V_G)/V_G$] due to the quadratic relationship between agradient flows and accelerations. In fact, it is apparent from Figs. 6d and 7b that while the agradient forces are pronounced in the eyewall, GWB could be satisfied to some degree as a useful approximation to the azimuthal-averaged tangential winds above the MBL. For example, the departures from GWB, increasing with altitude, are only about 2–5 m $s^{-1}$ with the relative errors of 3%–10% above the MBL (Fig. 7b), even though the relative agradient forces could range from 5% to 30% (as estimated from Figs. 6a,d). Note that the gradient departures of 1–5 m $s^{-1}$ in the eyewall are consistent with the root-mean-square error of 1.5 m $s^{-1}$ obtained by Willoughby (1990, 1991), when considering that his results were based on the observations taken only at 850 and 700 hPa. It is also apparent from Figs. 6d and 7b that agradient winds are similar in structure to agradient accelerations, indicating that *the former could be used as a measure of unbalanced acceleration.* Of interest is that the errors are smaller with cyclostrophic approximation (cf. Figs. 6c,d and Figs. 7a,b), indicating that this simpler approximation is as good as the GWB approximation in the eyewall. Obviously, GWB models could not reproduce the intense outflow jet near $V_{max}$, the deep radial outflows (with intense updrafts) in the eyewall, and particularly, the processes leading to the development of extensive outflows in the upper troposphere. These radial outflows result from the supergradient acceleration or the radial force imbalance in the eyewall, as discussed earlier. It should be pointed out that the general structures shown in Fig. 6 are still evident even after averaging over a period of 24 h, or after removing the asymmetric component of $PGF_R$ and horizontal winds (not shown).

Including the horizontal/vertical diffusion and surface friction has little impact on the above-mentioned agradient tendency structures, except in the MBL (Fig. 6d). For instance, numerical diffusion reduces (increases) slightly the supergradient tendency in the eyewall (eye). The surface friction and vertical turbulent fluxes act as a brake on the $PGF_R$-driven radial inflow in the lowest

1-km layer (Shapiro 1983) and the radial outflow immediately above near the RMW to produce a positive tendency below a negative tendency. Nevertheless, the net Lagrangian tendency does not depart significantly from the gradient imbalance, except in the MBL where the centrifugal braking effect on the radial inflow is enhanced (cf. Figs. 6d,f). This explains the relatively sharp deceleration of the low-level radial inflow as it approaches the RMW, and that little inflow can penetrate into the center of the eye above the surface layer.

Figure 8 shows the roles of radial and vertical advection in redistributing the radial Lagrangian tendencies. Obviously, radial advection tends to slow the low-level inward acceleration outside the peak radial inflow in the MBL and increases it inside (cf. Figs. 8a and 1b). Both radial and vertical advections are large and negative within the low-level outflow jet, consuming a substantial amount of the intense supergradient acceleration therein. In the eyewall, radial advection removes most of the local supergradient tendencies and enhances the radial outflow in the upper troposphere, whereas vertical advection tends to increase the local radial outflow above the updraft axis (inner portion) and reduce it below. As a result of the significant horizontal and vertical advections, the local tendency becomes one order of magnitude smaller than the Lagrangian tendency (cf. Figs. 8c and 6f). The local changes occur at a rate of $\pm 1$–2 m s$^{-1}$ h$^{-1}$, even at the upper- and low-level outflow layers where large supergradient acceleration is present. Moreover, the local tendencies show (a) the relatively slow intensification of the low-level inflow and upper-level outflow, (b) the tendency to develop a deep layer of outflow in the outer region below the melting-inflow layer (cf. Figs. 1b and 8c), and (c) the near-steady nature of the eye except above $z = 10$ km.

Figure 9 shows the asymmetric structures of Lagrangian tendencies and gradient wind departures in the eyewall. A deep layer of supergradient flows and forces is evident in the eyewall. They are similar in structure to each other, like their azimuthal averages, but their magnitudes are 2–3 times greater than the azimuthal averages. The supergradient winds exceed the gradient winds by 4–8 m s$^{-1}$ in the eyewall. Obviously, *the eyewall is unbalanced locally everywhere with dominant supergradient flows and forces.* Note that some supergradient flows take place in the midlevel inflow region as a result of the overshoot of tangential winds. However, most of the supergradient flows occur in the outflow region, evidently as a consequence of the upward transport of AAM by intense updrafts in the eyewall. Above the upper outflow layer, subgradient acceleration dominates, so radial inflows could develop with a magnitude similar to the local swirling winds (cf. Figs. 1b,c). There is also a shallow layer of subgradient tendencies above the MBL that appear to suppress the up- and outward expansion of the outflow jet (cf. Figs. 9 and 1b).

Since the agradient forces are accompanied by sig-

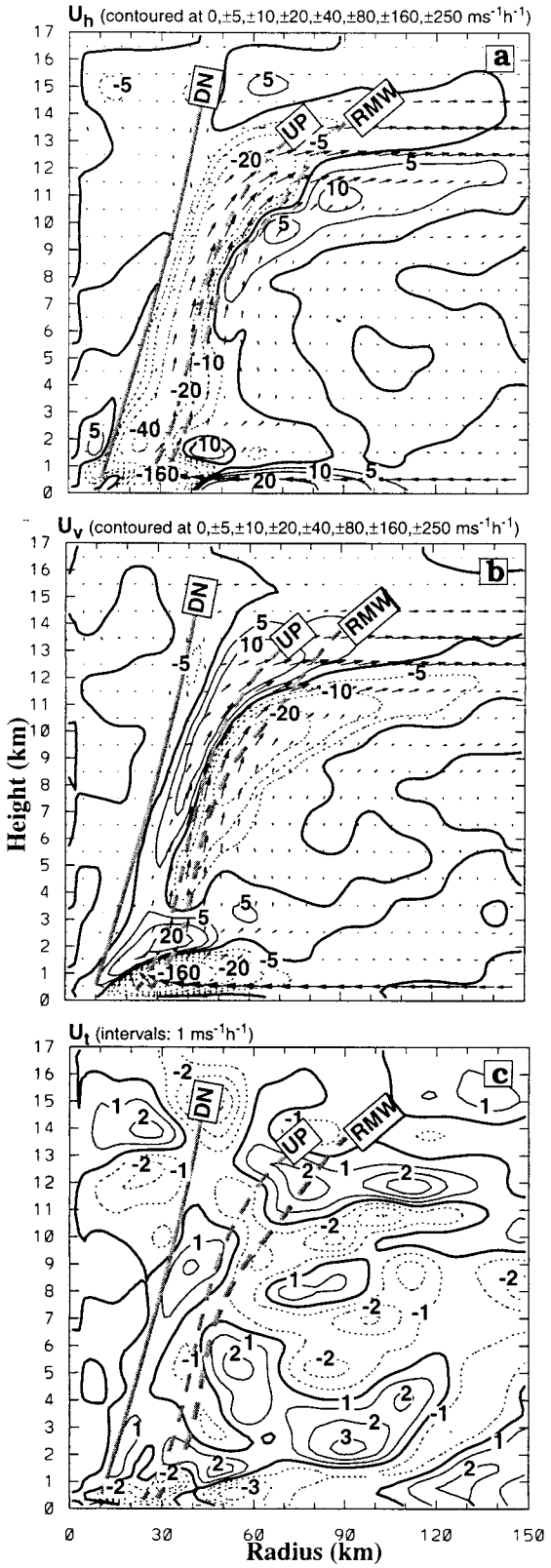


FIG. 8. As in Fig. 1 but for (a) horizontal advection ($U_H$), (b) vertical advection ($U_V$), and (c) local tendency ($U_t$) of radial momentum.

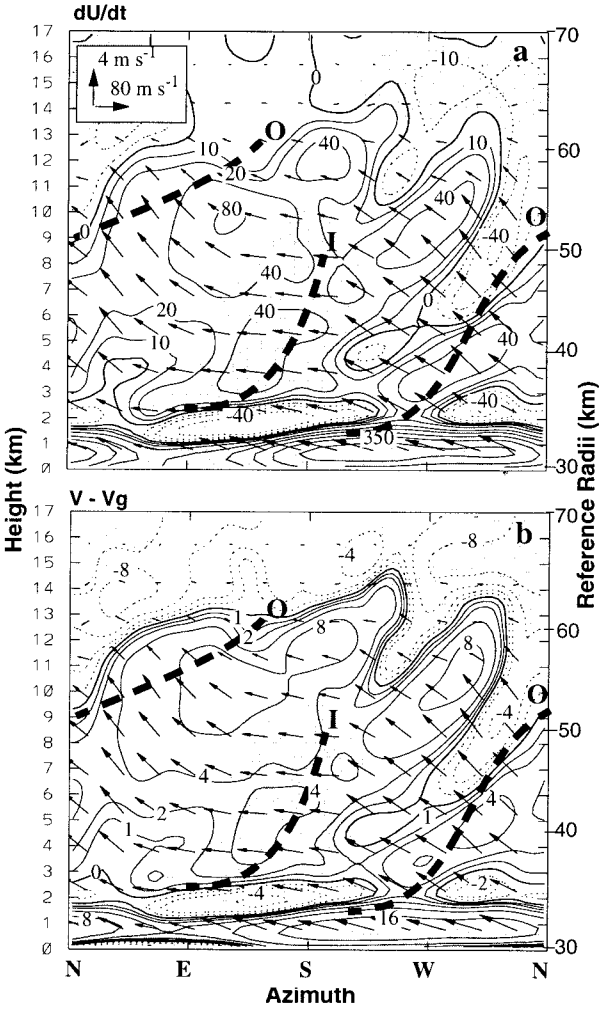


FIG. 9. As in Fig. 3a but for (a) the Lagrangian radial momentum tendency ($dU/dt$), contoured at 0, ±10, ±20, ±40, ±80, ±160, ±320, and ±350 m s$^{-1}$ h$^{-1}$; and (b) agradient winds ($V - V_g$), contoured at 0, ±1, ±2, ±4, ±8, and ±16 m s$^{-1}$. The inflow regions are shaded.

nificant radial flows and vertical motion, the unbalanced flows must appear as some types of azimuthally propagating waves in the baroclinic inner-core regions. However, little research has so far been performed to describe and understand the unbalanced flows in the eyewall. Previous theoretical studies discussed the radial propagation of inertial–buoyancy waves (e.g., Willoughby 1977, 1988; Xu 1983) and vortex–Rossby waves (e.g., Guinn and Schubert 1993; Montgomery and Kallenbach 1997) in relation to *spiral rainbands*, the azimuthal propagation of vortex–Rossby edge waves at the eye edge (Kuo et al. 1999), and buoyancy oscillations in the vertical motion *in the eye* (Liu et al. 1999). Thus, it is desirable to investigate what type of waves is associated with the unbalanced forces and flows in the eyewall. For this purpose, the instantaneous fields of radial flows $U'$ and accelerations $dU/dt$ are given in Fig. 10, which shows the wavenumber-2 structure in the eyewall but with different wavelengths. Note that these elements have been aliased to wavenumber-1 after the temporal average (cf. Figs. 10a and 3a). These downshear-tilted $U'$ wave ridges/troughs can be clearly traced at a time interval of 0.5–1.0 h (cf. Figs. 10a,b) in spite of the intense vertical shear, strong convective forcing, and wave dispersion. They each span roughly over a semicircle in the vertical. Of interest is that the wave ridges/troughs propagate cyclonically downstream and vertically upward (and radially outward) with an average slope of 1:16 well maintained in the slanting cross section. This implies that the bottom and upper portions of the wave ridges/troughs propagate at different speeds, namely, about 35 m s$^{-1}$ near the top of the MBL and about 60 m s$^{-1}$ at $z = 12$ km; they correspond roughly to half and twice the local swirling winds, respectively.

The above propagation characteristics appear to resemble those of azimuthally propagating vortex–Rossby waves. Specifically, the linear analysis of the (potential) vorticity wave on a Rankine vortex by Guinn and Schubert (1993) indicates that these waves should propagate at the phase speed ($c$) given by

$$c = V(1 - 1/m), \tag{7}$$

where $m$ is the azimuthal wavenumber. Equation (7) states that wavenumber $m = 1$ is stationary and wavenumbers $m = 2$, 3, and 4 move, respectively, at ½, ⅔, and ¾ the speed of the basic-state azimuthal flow. If we take $V = V_{max}$, as also suggested by Kuo et al. (1999), the linear theory describes well the azimuthal propagation of the $m = 2$ waves shown in Figs. 10a,b, at least to a first approximation. In this regard, the upper portion of the $U$' waves would appear to propagate ''passively'' with the wave at the $V_{max}$ level, and the top level of the MBL may be the origin of the vortex–Rossby waves.

Like the temporal average, the eyewall is again dominated by the areas of supergradient acceleration (Figs. 10c,d). The alternating agradient tendencies are exactly the manifestation of vortex–Rossby waves, and coincide closely with the perturbations in tangential winds (see Fig. 10 in Part II). Of importance is that the vortex–Rossby waves resemble in structure but lag roughly ¼ wavelength behind those of the radial flows. The correlation between radial inflows/outflows and the propagation of vortex–Rossby waves could be explained using the AAM transport in the eyewall. As discussed in Part II (in association with Fig. 10 therein), a phase relationship between the radial and tangential winds could be established as a result of the AAM transport by the eyewall updrafts. The resulting perturbations in tangential winds (or AAM) give rise to the vortex–Rossby waves. Because of the phase relationship, the leading (trailing) half portion of the radial flow waves tends to decrease (increase) in amplitude, thereby limiting the growth of the radial flows and leading to the upstream propagation of the vortex–Rossby waves with respect to the basic-state flow. This retrogressive character

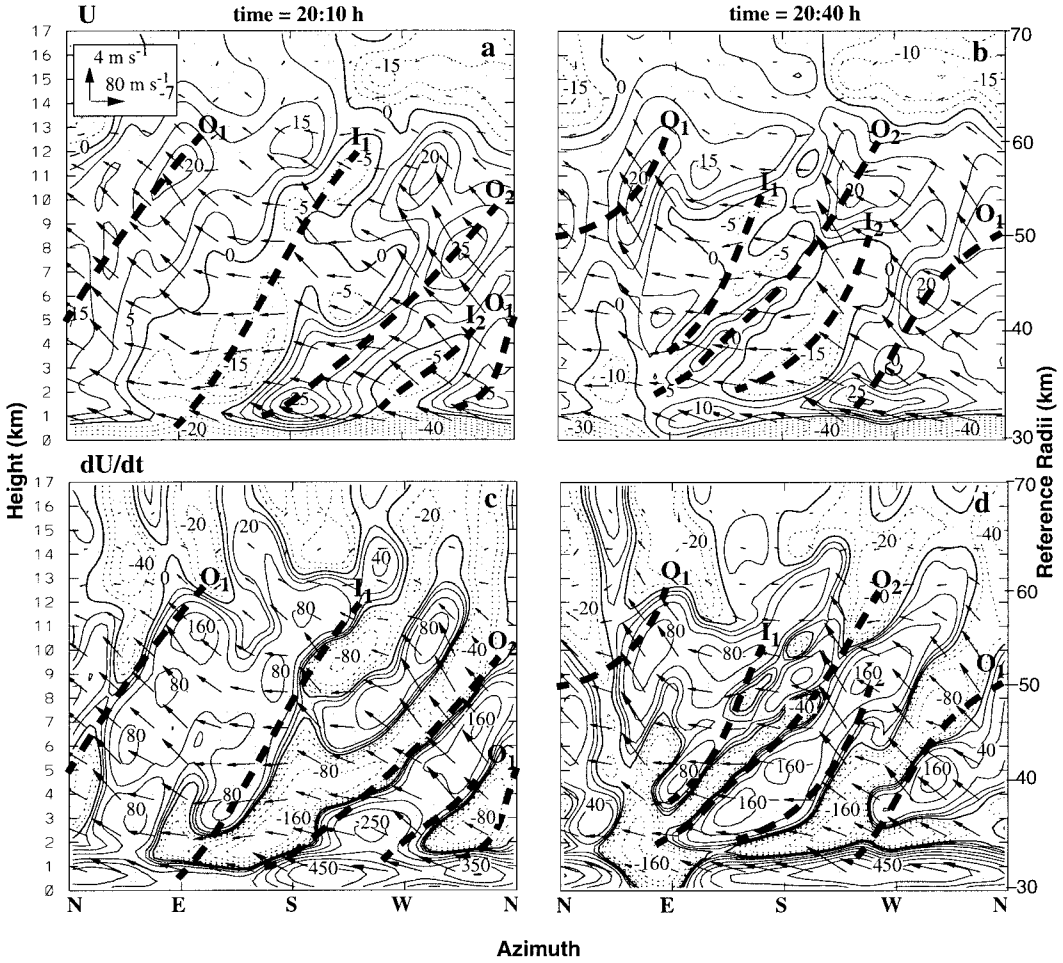


FIG. 10. As in Fig. 3a but for the instantaneous fields in the eyewall: (a) and (b) the system-relative radial flow (every 3 m $s^{-1}$) with the downdrafts shaded, and (c) and (d) the Lagrangian radial momentum tendency ($dU/dt$), contoured at 0, ±10, ±20, ±40, ±80, ±160, and ±320 m $s^{-1}$ $h^{-1}$, with the inflow shaded. The left and right panels are taken from the simulations valid at 2010 and 2040 UTC 23 Aug 1992, respectively.

could be readily described through the interaction of a (potential) vorticity anomaly with the basic flow (Guinn and Schubert 1993). Clearly, further theoretical and diagnostic studies are needed to address what determines the three-dimensional structures and propagation of the waves, and how they are related to the vertical shear, and the slope of the eyewall as well as the resolution of the model grid.

For the sake of completeness, we show in Fig. 11 the agradient forces in the eye that do not seem to be closely related to the radial flows, like the AAM budget. Although the upper and bottom portions of the tendencies change notably in response to the more intense radial flows, the basic structure is nearly upright in the vertical with the positive tendencies in the south semicircle most of the time. This structure is closely associated with the asymmetries in tangential winds (cf. Figs. 10b,c in Part II and Fig. 11 herein). Thus, it is not possible to use the present hurricane with a small eye to shed light on the unbalanced flows and asymmetric structures in the eye. Nevertheless, one may still see from Fig. 11 that there is little evidence on the formation of vortex–Rossby waves in the eye region, perhaps due to the absence of convective forcing or ''impulse'' in azimuthal flow (e.g., $V_{max}$). The eye region appears to be favorable for the generation of inertial gravity waves (Liu et al. 1999).

## 5. Summary and conclusions

In this study, we have examined the development of unbalanced *forces* and *flows* in the inner-core regions of a hurricane, through the analyses of prognostic radial momentum and AAM budgets, using a high-resolution (i.e., $\Delta x = 6$ km), fully explicit simulation of Hurricane Andrew (1992) with the PSU–NCAR nonhydrostatic model (i.e., MM5). More important results are summarized below.

- It is found from the AAM budgets that AAM is near-conserved three-dimensionally in the eyewall and that

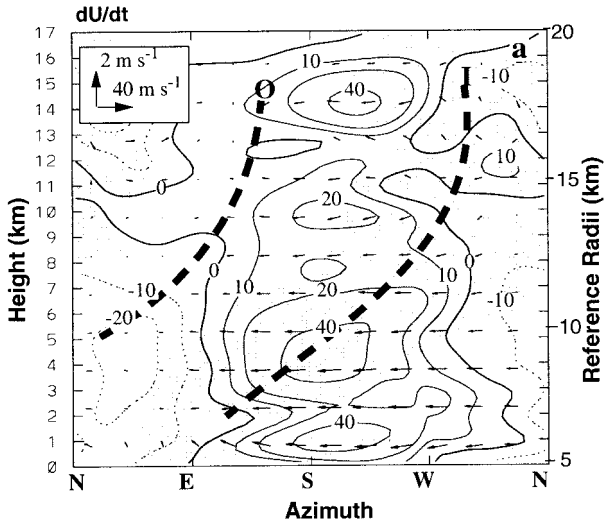


FIG. 11. As in Fig. 3b but for the Lagrangian radial momentum tendency ($dU/dt$) in the eye, contoured at 0, ±10, ±20, and ±40 m $s^{-1}$ $h^{-1}$, with the inflow shaded.

the MBL inflow is the major source of AAM for the spinup of the storm. The tangential winds in the eyewall could intensify not only in the inflow region as a result of the inward AAM transport, but also in the outflow region through the upward AAM transport when updrafts are intense. The system-averaged amplification depends on the excess of the upward AAM transport over that of radial transport in the eyewall. Because of the dominant intense updrafts in the eyewall, the upward transport of AAM tends to exceed the spindown effect of the outflow during the storm's deepening stage.

- The radial momentum budgets show that supergradient flows and forces, even after being temporally and azimuthally averaged, are well organized from the bottom of the eye center to the upper outflow layer in the eyewall, and their ridge axes above the MBL coincide with the core of the eyewall updrafts rather than the RMW. The eyewall is dominated by radial outflow and supergradient acceleration that is on average twice as large as the local Coriolis acceleration and varies from 5% to 30% of $PGF_R$ between $z = 2$ and 10 km. The intense outflow layer in the upper troposphere is formed as a result of continuous outward acceleration of airflows in the eyewall updrafts. The maximum imbalance with an outflow jet occurs in the vicinity of the peak tangential wind near the top of the MBL, and its supergradient tendency is as large as ⅓ of the centrifugal force. By mass continuity, this unbalanced outflow plays an important role in venting the air from the eye, thus leading to the reduction of the storm's central pressure. It is the centrifugal force that tends to prevent the MBL air from entering the eye and cause the supergradient acceleration above in the eyewall.
- There have been two different ways to estimate the gradient imbalance: one based on the unbalanced forces and the other on the departures from GWB. We have shown that despite the pronounced radial force imbalance (5%–30% of $PGF_R$) in the eyewall, GWB could still be satisfied within the 10% error to the azimuthally averaged tangential winds in most portions of the eyewall above the MBL. The relative error in agradient forces is roughly twice as large as that in agradient winds estimated from GWB when the flow is unbalanced. Furthermore, the simple cyclostrophic balance could be used as a reasonable approximation to the azimuthally averaged tangential winds above the MBL in the inner-core region. Our results appear to have resolved the controversial reports in the observational studies of Gray and Shea (1973) and Willoughby (1990). That is, their conclusions are both correct for the levels of observations they analyzed, because there are marked differences in the agradient forces and flows between the layers near the top of the MBL (where an outflow jet may be present) and the layers above.
- While agradient accelerations are pronounced in the eyewall, the local rate of changes in the primary and secondary circulations are both very small due to the effects of intense advections. The result suggests that the hurricane vortex flows evolve very slowly even during its rapid deepening stage.
- The azimuth–height cross sections of instantaneous fields display significant asymmetries but well-organized wavenumber-2 structures in the form of vortex–Rossby waves. These waves propagate cyclonically downstream and vertically upward (and radially outward). Their propagation speed varies with height and is half the tangential wind speed near the top of the MBL. The vortex–Rossby waves are shown to resemble in structure, but lag by ¼ wavelength behind, the radial flow waves, providing a retrogressive mechanism by which the vortex–Rossby waves move upstream with respect to the basic-state flow near the top of the MBL.

Based on the above results, the development of unbalanced flows in the eyewall during the intensifying stage could be readily understood as follows. As the storm deepens, the cross-isobaric radial inflow in the MBL transports more AAM from the hurricane environment into the eyewall region than frictional dissipation. The major radial inflow decelerates as it approaches the RMW where the centrifugal force exceeds $PGF_R$. The more the radius of the eyewall shrinks, the greater is the maximum tangential wind near the top of the MBL. Then, all the inflow air mass must ascend in the eyewall, transporting AAM upward to spin up the tangential flow above. This upward transport of AAM could increase significantly the local centrifugal force, thereby causing the pronounced supergradient acceleration and the development of radial outflow in the eyewall. In the present case, the supergradient acceleration

occurs at the same order of magnitude as $PGF_R$ in the vicinity of $V_{max}$, and accounts for the generation of an outflow jet near the top of the MBL. However, the local changes in tangential winds are always small due to the intense advection in the eyewall. It is evident that (a) the intensity of the radial outflow depends critically on the upward transport of AAM, and (b) the spindown of the eyewall by radial outflow must be overcompensated by the upward transport of AAM if the storm is to deepen. Of course, the underlying ocean (and latent heat release in the eyewall) is the fundamental energy source for the deepening of tropical cyclones.

It should be mentioned that the above results are obtained from an explicit simulation of a hurricane in which there are some deficiencies due partly to the lack of observations in specifying the model initial conditions and partly to the use of the 6-km grid size that is still too coarse to resolve deep convection in the eyewall. Nevertheless, many agreements between the simulated and the observed Andrew presented in Part I led us to the belief that the basic conclusions presented herein are relevant to real tropical storms.

*Acknowledgments.* We are grateful to Bill Kuo and Y.-R. Guo at NCAR/MMM for providing us some budget codes for an earlier version of the MM5. We are also grateful to Michael Montgomery and one anonymous reviewer for their critical comments that helped improve the quality of this paper significantly. This work was supported by NSF Grant ATM-9802391, NASA Grant NAG-57842, and ONR Grant N00014-96-1-0746. The computations were performed at the National Center for Atmospheric Research, which is sponsored by the National Science Foundation.

## REFERENCES

Dudhia, J., 1993: A nonhydrostatic version of the Penn State–NCAR mesoscale model: Validation tests and simulation of an Atlantic cyclone and cold front. *Mon. Wea. Rev.,* **121,** 1493–1513.

Eliassen, A., 1951: Slow thermally or frictionally controlled meridional circulation in circular vortex. *Astrophys. Norv.,* **5,** 19–60.

Emanuel, K. A., 1986: An air–sea interaction theory for tropical cyclones. Part I: Steady-state maintenance. *J. Atmos. Sci.,* **43,** 585–604.

——, 1997: Some aspects of hurricane inner-core dynamics and energetics. *J. Atmos. Sci.,* **54,** 1014–1026.

Gray, W. M., 1991: Comments on ''Gradient balance in tropical cyclones.'' *J. Atmos. Sci.,* **48,** 1201–1208.

——, and D. J. Shea, 1973: The hurricanes inner core region: Thermal stability and dynamic characteristics. *J. Atmos. Sci.,* **30,** 1565–1576.

Grell, G. A., J. Dudhia, and D. R. Stauffer, 1995: A description of the fifth generation Penn State/NCAR mesoscale model (MM5). NCAR Tech Note. NCAR/TN-398 + STR, 138 pp.

Guinn, T. A., and W. H. Schubert, 1993: Hurricane spiral rainband. *J. Atmos. Sci.,* **50,** 3380–3403.

Hawkins, H. F., and D. T. Rubsam, 1968: Hurricane Hilda, 1964. II. Structure and budgets of the hurricane on October 1, 1964. *Mon. Wea. Rev.,* **96,** 617–636.

Kuo, H.-C., R. T. Williams, and J.-H. Chen, 1999: A possible mechanism for the eye rotation of Typhoon Herb. *J. Atmos. Sci.,* **56,** 1659–1673.

Kuo, H.-L., 1959: Dynamics of convective vortices and eye formation. *The Atmospheric and Sea in Motion,* B. Bolin, Ed., Rockefeller Institute Press, 413–424.

LaSeur, N. E., and H. F. Hawkins, 1963: An analysis of Hurricane Cleo (1958) based on data from research reconnaissance aircraft. *Mon. Wea. Rev.,* **91,** 694–709.

Liu, Y., D.-L. Zhang, and M. K. Yau, 1997: A multiscale numerical study of Hurricane Andrew (1992). Part I: Explicit simulation and verification. *Mon. Wea. Rev.,* **125,** 3073–3093.

——, ——, and ——, 1999: A multiscale numerical study of Hurricane Andrew (1992). Part II: Kinematics and inner-core structures. *Mon. Wea. Rev.,* **127,** 2597–2616.

Malkus, J. S., 1958: On the structure and maintenance of the mature hurricane eye. *J. Meteor.,* **15,** 337–349.

Montgomery, M. T., and R. J. Kallenbach, 1997: A theory for vortex Rossby waves and its application to spiral bands and intensity changes in hurricanes. *Quart. J. Roy. Meteor. Soc.,* **123,** 435–465.

Raymond, D. J., 1992: Nonlinear balance and potential-vorticity thinking at large Rossby number. *Quart. J. Roy. Meteor. Soc.,* **118,** 987–1015.

Schubert, H. V., and J. J. Hack, 1982: Inertial stability and tropical cyclone development. *J. Atmos. Sci.,* **39,** 1687–97.

Shapiro, L. J., 1983: The asymmetric boundary layer flow under a translating hurricane. *J. Atmos. Sci.,* **40,** 1984–1998.

——, and H. E. Willoughby, 1982: The response of the balanced hurricanes to local sources of heat and momentum. *J. Atmos. Sci.,* **39,** 378–394.

——, and M. T. Montgomery, 1993: A three-dimensional balance theory for rapidly rotating vortices. *J. Atmos. Sci.,* **50,** 3322–3335.

Smith, R. K., 1980: Tropical cyclone eye dynamics. *J. Atmos. Sci.,* **37,** 1227–1232.

Willoughby, H. E., 1977: Inertia-buoyancy waves in hurricanes. *J. Atmos. Sci.,* **34,** 1028–1039.

——, 1979: Forced secondary circulations in hurricanes. *J. Geophys. Res.,* **84,** 3173–3183.

——, 1988: The dynamics of the tropical cyclone core. *Aust. Meteor. Mag.,* **36,** 183–191.

——, 1990: Gradient balance in tropical cyclones. *J. Atmos. Sci.,* **47,** 265–274.

——, 1991: Reply. *J. Atmos. Sci.,* **48,** 1209–1212.

Xu, Q., 1983: Unstable spiral inertial gravity waves in typhoons. *Sci. Sin.,* **26,** 70–80.

Zhang, D.-L., Y. Liu, and M. K. Yau, 2000: A multiscale numerical study of Hurricane Andrew (1992). Part III: Dynamically induced vertical motion. *Mon. Wea. Rev.,* **128,** 3772–3788.